Mesoporous MoO₃₋ₓ Material as an Efficient Electrocatalyst for Hydrogen Evolution Reactions

Zhu Luo, Ran Miao, Tran Doan Huan, Islam M. Mosa, Altug S. Poyraz, Wei Zhong, Jacqueline E. Cloud, David A. Kriz, Srinivas Thanneeru, Junkai He, Yashan Zhang, Rampi Ramprasad, and Steven L. Suib*

A unique approach for the synthesis of nonstoichiometric, mesoporous molybdenum oxide (MoO₃₋ₓ) with nanosized crystalline walls by using a soft template (PEO-*b*-PS) synthesis method is introduced. The as-synthesized mesoporous MoO₃₋ₓ is very active and stable (durability > 12 h) for the electrochemical hydrogen evolution reaction (HER) under both acidic and alkaline conditions. The intrinsic MoO₃ serves as an HER electrocatalyst without the assistance of carbon materials, noble metals, or MoS₂ materials. The results from transmission electron microscopy and N₂ sorption techniques show that the as-synthesized mesoporous MoO₃₋ₓ has large accessible pores (20–40 nm), which are able to facilitate mass transport and charge transfer during HER. In terms of X-ray diffraction, X-ray photoelectron spectroscopy, temperature-programmed oxidation, and diffusive reflectance UV–vis spectroscopy, the mesoporous MoO₃₋ₓ exhibits mixed oxidation states (Mo⁵⁺, Mo⁶⁺) and an oxygen-deficient structure. The as-synthesized MoO₃₋ₓ only requires a low overpotential (≈0.14 V) to achieve a 10 mA cm⁻² current density in 0.1 M KOH and the Tafel slope is as low as 56 mV dec⁻¹. Density functional theory calculations demonstrate a change of electronic structure and the possible reaction pathway of HER. Oxygen vacancies and mesoporosity serve as key factors for excellent performance.

1. Introduction

Hydrogen has been intensively pursued as a future energy carrier due to its renewable and environmentally friendly properties compared to other fuels (coal, gasoline, methane, etc.). Growing attention has been paid to the sustainable hydrogen evolution reaction (HER) from the water splitting reaction, which is a clean and environmentally benign reaction pathway. Usually, HER in acidic media requires lower overpotential, which is more economically efficient compared to alkaline media reaction. Alkaline media is still promising due to the possibility for driving the overall water splitting reaction by producing hydrogen at the cathode and oxygen at the anode simultaneously.[1,2]

Pt and Pt-based materials are known as the most efficient electrocatalysts for HER in both acidic and alkaline conditions. However, the scarcity and high cost of Pt do not allow the widespread use as electrocatalysts for HER. The development of electrocatalysts that are Pt free, highly active, and operable in both acidic and alkaline conditions remains a challenging task. In recent years, metal sulfides (MoS₂, FeS₂, etc.),[3,4] carbon-based (carbon nanotubes, graphitic carbon, etc.)[5] or hybrid materials (carbon supported metal oxide, reduced graphene oxide supported metal sulfides, etc.)[6,7] have been intensively studied as replacements for Pt-based electrocatalysts. These materials have been reported that have high active HER activity and stability in acidic media or alkaline media. Nevertheless, electrocatalysts that could drive HER in both acidic and alkaline systems were rarely reported in the literature. More studies need to be done to understand the catalytic activity and the chemical stability under different conditions.

Molybdenum-based materials (such as molybdenum carbonitride (MoCN), molybdenum diselenide (MoSe₂), and bimetallic Ni–Mo–C materials) have been investigated as active HER electrocatalysts.[8–10] Molybdenum disulfides (MoS₂) are Mo-based materials that have been widely studied and have exhibited promising HER activity.[11] In 2005, Hinnemann et al. first reported that the undercoordinated sulfur atoms at the edges of MoS₂ have very similar properties to natural HER active enzymatic centers.[12] Since then, MoS₂ materials have been extensively investigated for HER. However, its catalytic HER activity is limited by the number of active sites.

Z. Luo, Dr. T. D. Huan, W. Zhong, Dr. J. E. Cloud, J. He, Prof. R. Ramprasad, Prof. S. L. Suib
Institute of Materials Science, U-3136
University of Connecticut
Storrs, CT 06269, USA
E-mail: steven.suib@uconn.edu
R. Miao, I. M. Mosa, Dr. A. S. Poyraz, D. A. Kriz, S. Thanneeru, Dr. Y. Zhang, Prof. S. L. Suib
Department of Chemistry, U-3060
University of Connecticut
Storrs, CT 06269-3060, USA
I. M. Mosa
Department of Chemistry
Tanta University
Tanta 31527, Egypt

Molybdenum oxide (MoO_3) is a low cost, nontoxic and environmentally benign transition metal with high stability. MoO_3 is widely employed in heterogeneous catalysis, electrocatalysis, and also in capacitors, and lithium-ion battery applications.[13–15] The orthorhombic α-MoO_3 (thermodynamically stable phase) has a layered structure which is formed by stacking bilayer sheets of MoO_6 octahedra with van der Waals forces.[16] This structure is suitable for insertion/removal of small ions such as H^+, and therefore is intensively studied as a supercapacitor. However, without active edges like those of MoS_2, intrinsic MoO_3 material has not been reported as an electrocatalyst for HER to the best of our knowledge.

Herein, we are reporting that mesoporous MoO_{3-x} serves as an active HER electrocatalyst under both alkaline and acidic conditions, without any extrinsic dopants, alloys, or any hybrid metals. The HER activity of MoO_3 has been developed and improved by considering the following aspects. First is the mesoporosity of MoO_3, since the mesoporous structure was shown previously to effectively enhance the activity of various kinds of metal oxides (WO_3, TiO_2, Co_3O_4, etc.) in catalytic reactions.[17–20] Second is the design of nonstoichiometric MoO_{3-x} with oxygen vacancies. The oxygen deficient structure has been manifested in other transition metal oxides (TMOs; TiO_2, WO_3, ZnO, MnO_2, etc.) that are able to facilitate charge transfer, mass transport, and narrowing bandgaps in various catalytic reactions.[21–24] The potential effects of oxygen vacancies of TMOs are significant in an HER system. Wu et al. described a novel approach to prepare WO_2-carbon mesoporous materials with high concentration of oxygen vacancies. They effectively proved the mesostructure and oxygen vacancies are important parameters for outstanding HER performance.[6] The last design is the phase of MoO_3, where orthorhombic α-MoO_3 (thermodynamically stable phase) has a layered structure which is suitable for insertion/removal of small ions such as H^+ in electrochemical

reactions.[25,26] Based on the above designs, the synthesis mechanism of mesoporous, oxygen deficient MoO_{3-x} is proposed schematically in **Scheme 1**. Unlike traditional preparation methods of mesoporous materials, the metal precursor used in this study is the commercial molybdenum trioxide (molybdite), which will be named *com*MoO_3 is relatively cheap and abundant. Firstly, *com*MoO_3 powder is added to H_2O_2 solution. The MoO_3 powder can be completely dissolved and results in a transparent yellow solution, with the formation of the solution-soluble precursor compound $MoO_2(OH)(OOH)$.[27]

By further combining with the soft template (PEO-*b*-PS), the preparation process is flexible, effective, and easy to control. Tetrahydrofuran (THF) is chosen as a solvent due to the ability to dissolve non-Pluronic copolymers such as PEO-*b*-PS. Both PS and PEO blocks can be completely dissolved without self-assembly aggregation (Scheme 1, step 1). Water is a selectively poor solvent for the PS block. With the mixing of water based Mo precursor and THF dissolved PEO-*b*-PS, inverse micelles with PEO cores and PS coronas are formed in solution (step 2). The coordination interaction between hydrophilic PEO and the Mo source thus triggers the self-assembly to form ordered polymer-oxide hybrids. After solvent evaporation (condensation process), two neighboring micelles fuse together and permanent Mo-O covalent bonds can be formed between PEO domains (step 3) in the hybrid. The powder X-ray diffraction (PXRD) (Figure S1a, Supporting Information) and Raman spectroscopy (Figure S1b, Supporting Information) characterization methods were employed to studied the covalent bonds in the as-prepared Mo hybrid sample. The organic block polymer can be burned off following thermal calcination. With an increasing of calcination temperature, the Mo crystals grow and expand to form connected intraparticle voids, which are mesopores (step 4). A critical temperature for the phase transition of MoO_3 is 350 °C. For MoO_3 samples calcined less
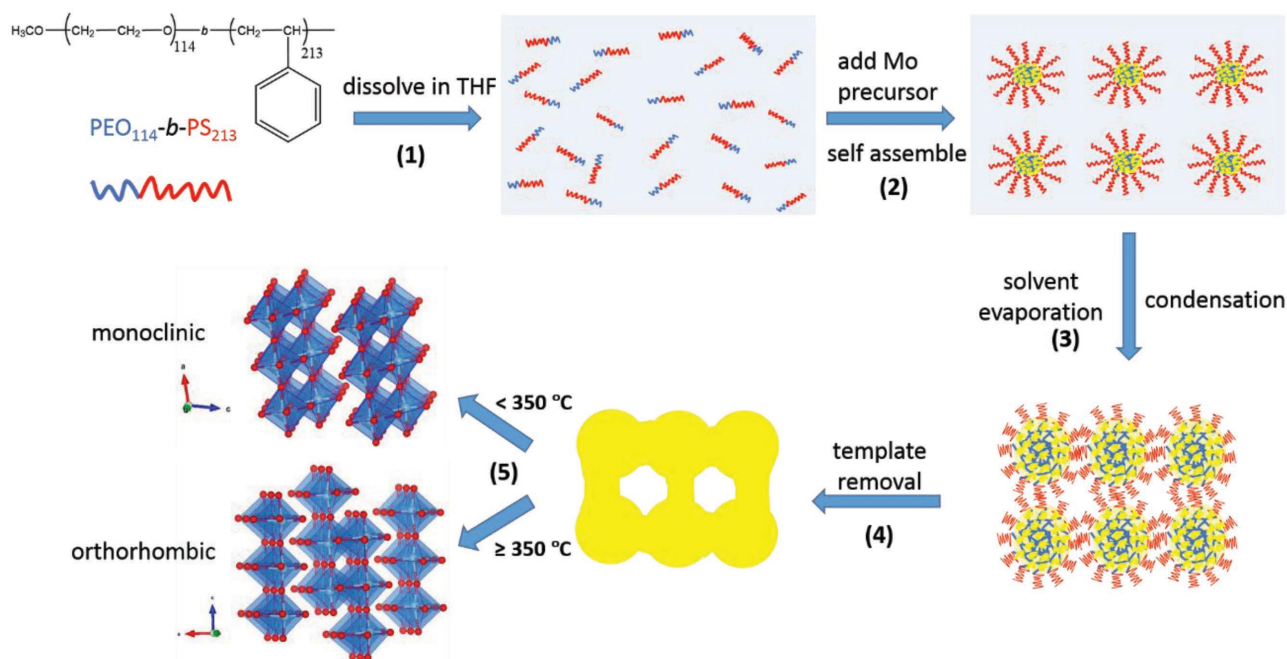
Scheme 1. The proposed formation mechanism of inverse micelle–templated mesoporous MoO_{3-x}.

www.MaterialsViews.com

ADVANCED
ENERGY
MATERIALS
www.advenergymat.de

FULL PAPER

than 350 °C, monoclinic β-MoO$_3$ is the dominant phase. Crystallization to the more thermodynamically stable orthorhombic α-MoO$_3$ occurs at 350 °C and above.[28] Above all, we are reporting mesoporous MoO$_{3-x}$ material as an efficient HER catalyst under both acidic and alkaline conditions. Our experimental and theoretical (density functional theory (DFT) calculation) results indicate that the soft-template synthesis of TMOs with mesoporosity and oxygen deficiency provides a promising strategy for electrochemical energy conversion and storage applications.

2. Results

2.1. Catalyst Characterization

In order to study the crystal phase change during the synthesis of mesoporous MoO$_3$ (mMoO$_3$), PXRD and Raman spectroscopy were used. Shown in **Figure 1**a, for the as-synthesized mMoO$_3$, all the diffraction lines could be assigned to the orthorhombic phase (α-MoO$_3$ phase, JCPDS No. 05-0508), which is crystallized in a layered structure composed of MoO$_6$ octahedra by sharing edges and corners. The commercial MoO$_3$ (comMoO$_3$) sample also shows the orthorhombic phase (α-MoO$_3$ phase, JCPDS No. 35-0609), but with different crystal parameters. No diffraction lines of other phases (β-MoO$_3$, h-MoO$_3$) were found in both samples. The mMoO$_3$ shows much lower crystallinity than comMoO$_3$, which may be due to the formation of a mesoporous structure that breaks the long-term crystallinity. Another observation is that for synthesized mMoO$_3$, the relative diffraction intensity between (040) and (021) planes is significantly different for comMoO$_3$, which indicates a preferred crystal orientation along the [001] direction.[29] PXRD is not sensitive to detect the carbon material. The possible existence of carbon and the chemical changes in mMoO$_3$ samples were analyzed using Fourier transform infrared spectra, shown in Figure S2 in the Supporting Information. Compared to Mo hybrid samples, no obvious carbon signals can be detected in mMoO$_3$ samples, suggesting most of the carbon species were removed by thermal treatment. The phase of molybdenum oxide samples can be further characterized by Raman spectroscopy (Figure 1b), due to each phase occupying different atomic arrangements with different Raman vibrational bands.

The three characteristic vibrational modes of the orthorhombic phase at 289, 818, and 995 cm^{-1} are observed for both samples.[30] All observed vibrational modes are in agreement with the α-MoO$_3$ phase reported in the literature.[31] Based on PXRD and Raman results, even though the introduction of PEO-b-PS surfactant slightly decreased the crystallinity of MoO$_3$, the thermodynamic stable orthorhombic phase (α-MoO$_3$) was preserved during the formation of the mesostructure. The presence of mesopores could be further manifested by SEM, TEM, and N$_2$ sorption techniques.

Figure 2a–c shows field-emission scanning electron microscopy (FESEM) images for the mesoporous molybdenum (mMoO$_3$) sample with various magnification scales. In terms of SEM results, the mMoO$_3$ sample is composed of small particles, which have sizes smaller than 100 nm. The porosity was formed by the aggregation of nanoparticles, and the pores are the connected intraparticle voids. With lower magnification images (Figure 2c), it is easier to observe the good dispersion of the pores. For comparison, the SEM image of comMoO$_3$ sample was also recorded (Figure 2d). The commercial sample is composed of a giant chunk of crystal (5–10 μm) instead of nanoparticles. No porosity could be observed in this sample.

Transmission electron microscopy (TEM) was used to further examine particle size, morphology, porosity, and crystallinity. In a typical TEM image shown in Figure 2e, the particle size of mMoO$_3$ is in the range of 50–100 nm, in accordance with SEM results. The mMoO$_3$ has a porous structure. Most of the pores are in the range of mesopores (20–40 nm). These mesopores are not of a uniform shape, but well dispersed between nanoparticles. In a higher magnification image (Figure 2e, onset image), a typical mesopore connected with crystalline particles with a diameter around 30 nm is clearly observed. In Figure 2f, the measured d-spacing ($\approx$0.35 nm) corresponding to the (040) planes of the α-MoO$_3$ phase, which is in accordance with XRD and Raman results. The specific pore size distribution was further confirmed by using N$_2$ sorption techniques. Figure S3a (Supporting Information) shows nitrogen sorption isotherms of mMoO$_3$ and comMoO$_3$ materials. The isotherm of mMoO$_3$ is categorized as Type IV, with a distinct hysteresis loop observed in the pressure range of 0.5–1 p/p_0, indicating the mesoporosity of the material. The isotherm of comMoO$_3$ manifests its nonporous property, without an obvious hysteresis loop. Figure S3b (Supporting Information) shows the
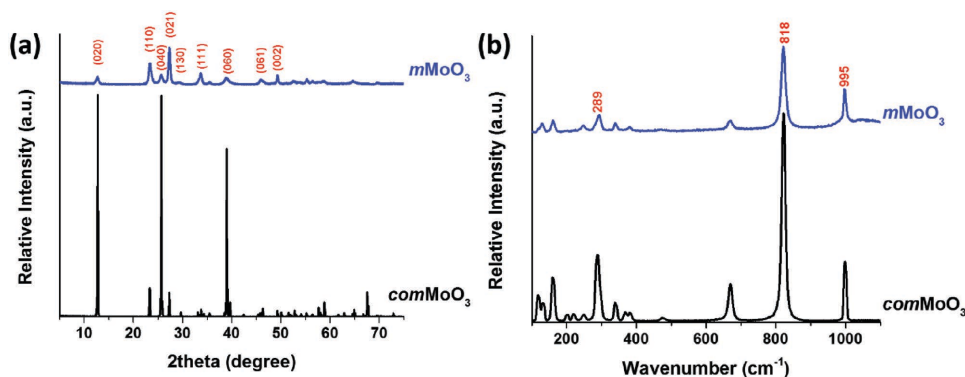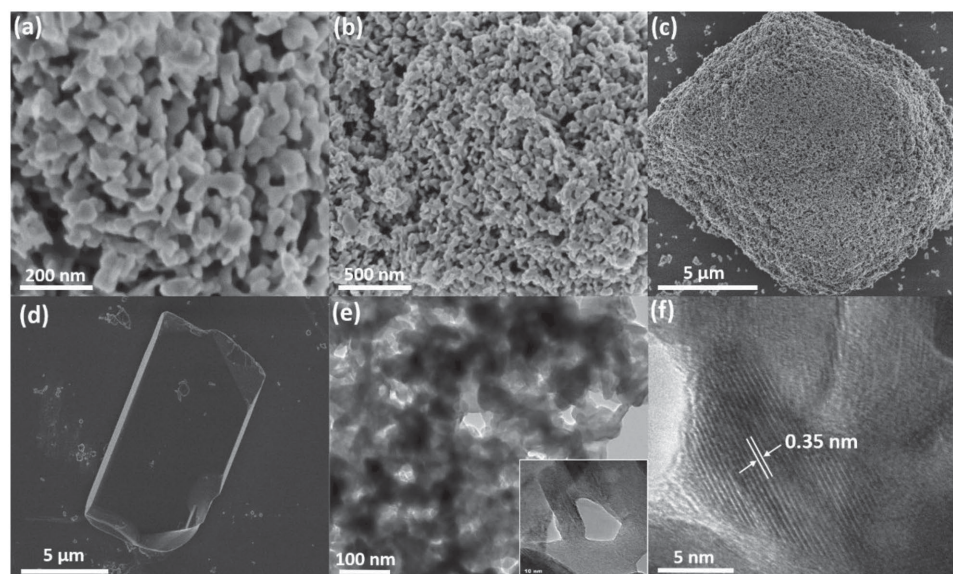

Figure 1. a) Powder X-ray diffraction patterns and (b) Raman spectroscopy for comMoO$_3$ (black pattern) and mesoporous mMoO$_3$ (blue pattern).

Figure 2. Scanning electron microscopy (SEM) images for mesoporous mMoO$_3$ sample with different magnifications. Porosity could be observed with different scales: a) 200 nm, b) 500 nm, and c) 5 µm. d) The SEM image of comMoO$_3$ as a comparison. e) The transmission electron microscopy (TEM) image of mMoO$_3$ with well dispersed mesopores (20–40 nm), a typical mesopore is illustrated in the onset image with a scale bar of 10 nm. f) High-resolution TEM of mMoO$_3$, the d-spacing (0.35 nm) of (040) plane of α-MoO$_3$ is displayed.

corresponding Barrett–Joyner–Halenda (BJH) pore size distribution of mMoO$_3$, with an average pore diameter of 31 nm, in good accordance with SEM and TEM results. Moreover, the as-synthesized mMoO$_3$ has a much larger surface area (52 m^2 g^{-1}) than comMoO$_3$ (2 m^2 g^{-1}). With a larger surface area, an improved catalytic activity is expected.

Besides mesoporosity, the oxidation state of the metal and surface oxygen deficiencies are also important properties for TMOs. To elucidate the oxidation state of the comMoO$_3$ material and the mesoporous MoO$_3$ material, X-ray photoelectron spectroscopy (XPS) measurements were applied. **Figure 3**a exhibits the Mo 3d XPS core spectra of the as-prepared mMoO$_3$ and comMoO$_3$. The Mo 3d core level spectrum of the comMoO$_3$ (lower curve) consists of a spin orbit doublet with peaks at 235.6 and 232.4 eV, which are attributed to 3d$_{3/2}$ and 3d$_{5/2}$ of the Mo cations in high oxidation states (Mo^{6+}). Without the

observation of other valence states, comMoO$_3$ possesses a fully stoichiometric structure according to PXRD and XPS results, which are consistent with previous reports.[27] However, for the mMoO$_3$ sample, an obvious shift to lower binding energy can be observed. Without changing the energy difference ($\Delta = 3.2$ eV) between the two peaks, Mo 3d$_{3/2}$ shifted to 234.4 eV and Mo 3d$_{5/2}$ shifted to 231.2 eV. Both of these two peaks can be assigned to Mo^{5+} species.[32] The presence of Mo^{5+} cations leads to an increment in electron density and a weaker binding effect. Figure 3b shows the O 1s spectra, for the comMoO$_3$ material (lower curve). No obvious shift is observed, all peak positions are in good agreement with literature values: the main component peak at 531.3 eV (blue curve) corresponds to lattice oxygen (O^{2-});[33] the other two component peaks (533.1 and 534.6 eV) are attributed to surface adsorbed species (OH$^-$, O$^-$).[34,35] On the contrary, the major O 1s peak of mMoO$_3$ shifted to a much
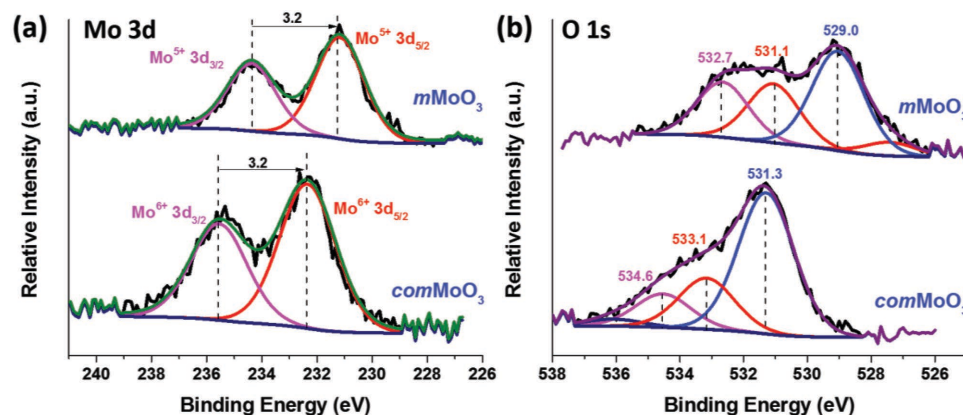
Figure 3. XPS spectrum details for (a) Mo 3d binding energy regions and (b) O1s level. Lower and upper curves are comMoO$_3$ and as-synthesized mMoO$_3$, respectively.

lower level (529 eV), which indicates a change in the coordination configuration of Mo with O. As reported, the O 1s shifts to a lower energy level in line with the transfer of electrons to the neighboring oxygen vacancies.[36] The presence of oxygen vacancies is suggested. Binding energy shifts to lower energy levels was also reported in other oxygen-deficient TMOs, such as the most widely studied material, TiO_{2-x}.[37] We could exclude the possibility of shifts coming from instrumental error, since the position of an internal standard (C 1s) peak is observed at 284.5 eV for both materials without any shifts (Figure S4, Supporting Information).

Another evidence that indicates the presence of oxygen vacancies is the color change (**Figure 4**a onset images). The comMoO$_3$ possesses a light greenish color, while the as-synthesized mMoO$_3$ has a blue color. Similar to the case with oxygen-deficient WO_{3-x} and TiO_{2-x}, the blue color of the TMO originates from characteristic outer d-shell electrons.[38,39] In this study, the as-synthesized blue molybdenum oxide species are quite stable in a sealed vial and could maintain their original color for at least 1 year. Moreover, the optical properties of molybdenum oxides are strongly affected as a function of the oxygen vacancy concentration.[40,41] Thus, diffuse reflectance ultraviolet–visible (DR UV–vis) spectra were measured. In Figure 4a, the comMoO$_3$ (black curve) shows a major absorption band in the UV range (< 410 nm) and a cutoff wavelength at 420 nm, indicating an optical band gap around 2.96 eV (detailed calculation in Supporting Information). The mMoO$_3$ shows a new and broad absorption band in the visible range

(>410 nm), which means a much smaller band gap than for comMoO$_3$. Since there are no extrinsic dopants in the mMoO$_3$ system, the narrowing of the band gap could be ascribed to the presence of oxygen vacancies.

The existence of oxygen vacancies was further investigated by oxygen temperature-programmed oxidation (TPO). The O_2 TPO profiles of mMoO$_3$ and comMoO$_3$ are compiled in Figure 4b. The O_2 TPO profile of comMoO$_3$ (black curve) exhibits no obvious oxygen consumption peaks, indicating no oxygen vacancies on the surface of comMoO$_3$. While the O_2 TPO profile of mMoO$_3$ shows a predominant oxygen consumption peak around 460 °C, suggesting the existence of oxygen vacancies in the mMoO$_3$ sample, which are able to react with flowing oxygen. Both samples after O_2 TPO treatment were collected (onset images in Figure 4b). A significant color change of mMoO$_3$ was observed. The mMoO$_3$ lost its original blue color, due to oxygen vacancies that were filled by the oxygen flow. As a comparison, no color change is noticed with the comMoO$_3$ sample.

With further studies, DFT calculations were applied to analyze the band structure of MoO$_3$ with and without oxygen vacancies. Figure 4c shows that with oxygen vacancies in different sites (V1, V2, and V3), a much smaller band gap could be obtained compared to MoO$_3$ without any oxygen vacancies (detailed calculations in Supporting Information). The smaller band gap observation is in agreement with the results from DR UV–vis spectroscopy. The α-MoO$_3$ has a layered structure with three different sites of oxygen that can form vacancies, as
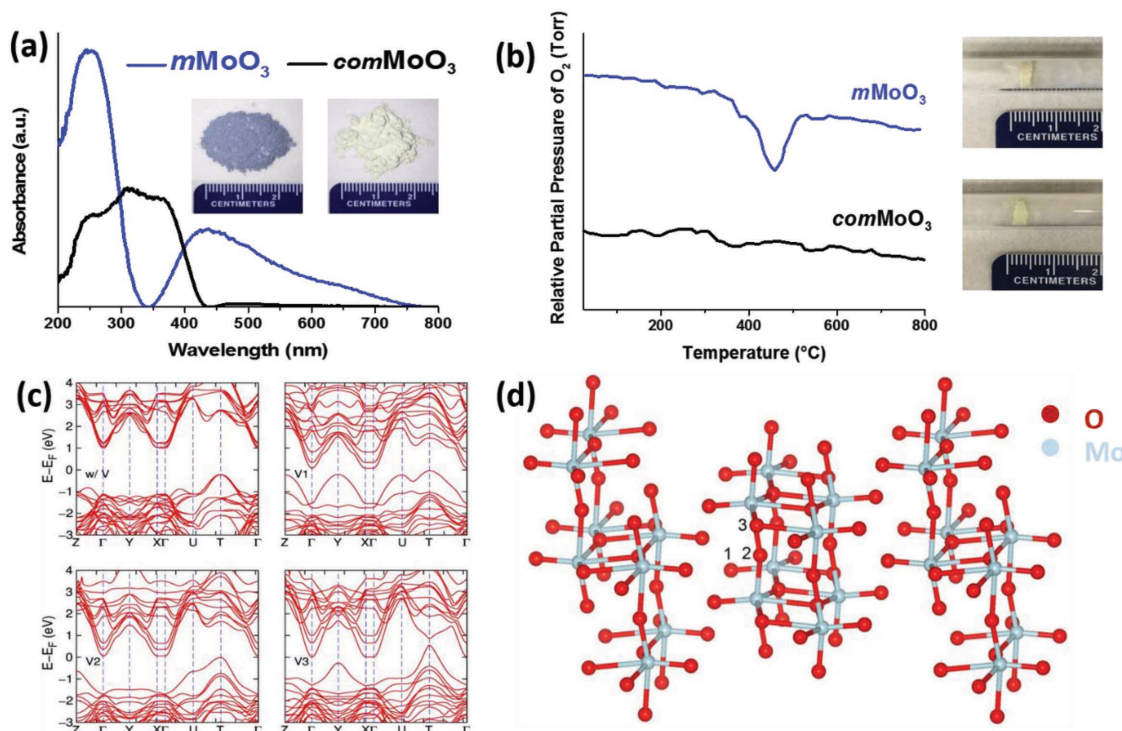
Figure 4. a) Diffuse reflectance ultraviolet–visible spectra (DR UV–vis) and photos (onset images) for comMoO$_3$ and as-synthesized mMoO$_3$. b) Oxygen temperature-programmed oxidation (TPO) for comMoO$_3$ and mMoO$_3$ samples. The onset images display the color change of samples after TPO treatment. c) Electronic band structure of orthorhombic MoO$_3$ without (w/ V) and with (V1, V2, and V3) vacancies at different sites. d) Optimized structure of MoO$_3$ in which Mo and O atoms are shown in cyan and red colors. Numbers (1, 2, and 3) indicate three different positions of O which are considered for vacancies.

shown in Figure 4d. A vacancy at site 1 is most thermodynamically stable. We then considered the effects of oxygen vacancies at site 1 (detailed calculations in Supporting Information).

2.2. HER Catalytic Activity and Stability Test

The electrocatalytic activities of the as-synthesized $mMoO_3$ materials were examined in both alkaline (0.1 M KOH, **Figure 5**a–c) and acidic aqueous (0.1 M H_2SO_4, Figure 5d–f) solutions. All materials tested in alkaline solution were deposited onto 3D nickel foam, which acts as a large surface area working electrode. Due to the instability of Ni in acidic solutions, carbon cloth (C cloth) was used as the working electrode in H_2SO_4 solution. For comparison, bare Ni foam, bare C cloth, $comMoO_3$, and commercial 20 wt% Pt/C were also studied under identical conditions. Figure 5a shows the HER polarization curves of various electrocatalysts in 0.1 M KOH solution. Bare Ni foam (black curve) requires a large overpotential (≈314 mV) to achieve a 10 mA cm^{-2} HER current density. The $comMoO_3$, which was loaded on Ni foam, performed similarly as bare Ni foam (blue curve). No improvement can be observed for the HER activity. For as synthesized $mMoO_3$ samples, the current densities reach 10 mA cm^{-2} at potentials of 138 mV. This overpotential value is much closer to the Pt/C catalyst system (η = 52 mV for j = −10 mV cm^{-2}) as compared to bare Ni or commercial sample tested under identical conditions, indicating enhanced catalytic activity in mesoporous sample

($mMoO_3$). Moreover, the HER activity of $mMoO_3$ sampler after O_2 TPO treatment ($mMoO_3$-T) was also examined. With an overpotential value at 273 mV, the $mMoO_3$-T sample shows a much lower activity than $mMoO_3$. Additionally, in order to exclude the effects from Ni foam, the $mMoO_3$ and $comMoO_3$ samples were deposited on glassy carbon (GC) electrodes and tested in 0.1 M KOH for HER performance. In Figure S9 (Supporting Information), the bare GC electrode shows almost no catalytic activity for HER. The $mMoO_3$ sample still shows much higher activity than the $comMoO_3$ sample.

Besides activity, stability is another major concern for all electrocatalysts. The electrochemical stability of $mMoO_3$ was evaluated by monitoring the current density during continuous operation at −0.174 V (vs reversible hydrogen electrode (RHE)) under alkaline conditions. The current density versus time data provided in Figure 5b show that the value remains stable after a slight initial increase in the beginning several hours. The current density does not vary significantly in 12 h, manifesting excellent stability of mesoporous MoO_3 during the electrochemical experiments. The onset SEM images were taken before and after a stability test of $mMoO_3$ sample (higher resolution images in Figure S5, Supporting Information). The unchanged morphology further suggested the stability of the catalyst. The crystal phase and the oxidation states of $mMoO_3$ after stability tests were further examined by Raman spectroscopy (Figure S6, Supporting Information) and XPS (Figure S7, Supporting Information), no obvious changes were observed.
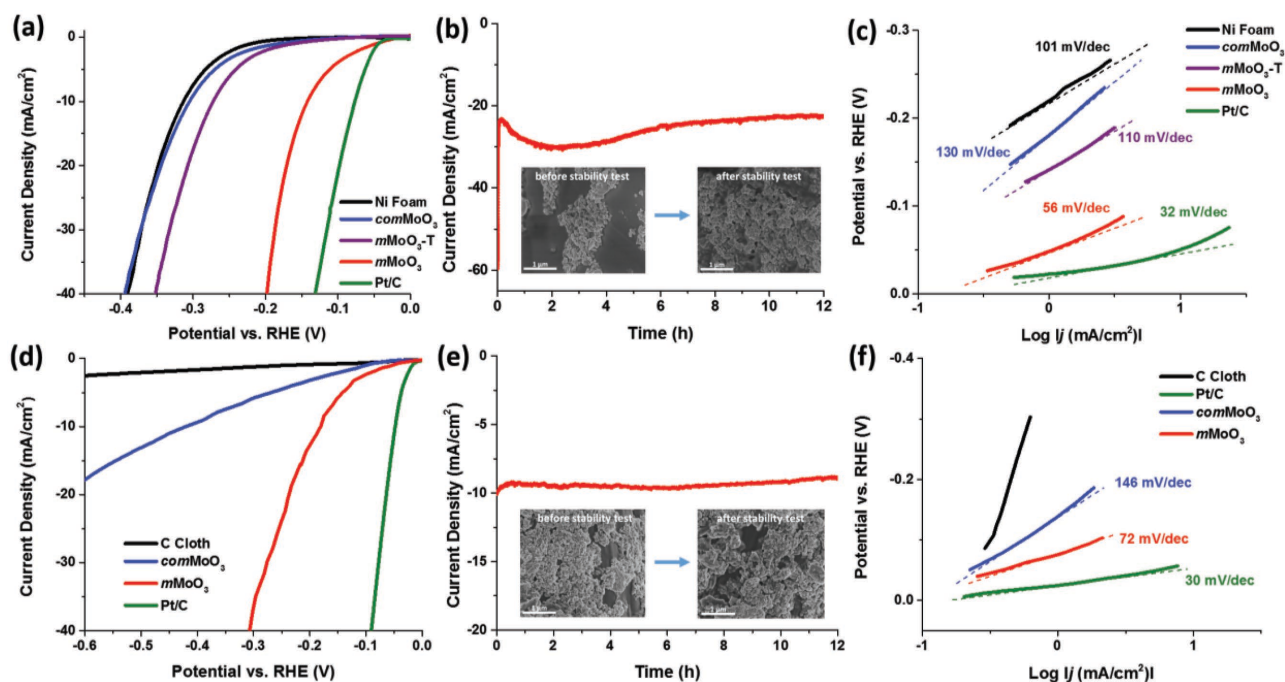
Figure 5. a) Polarization curves of $mMoO_3$ materials on Ni foam electrode in 0.1 M KOH, along with bare Ni foam, $comMoO_3$, $mMoO_3$-T, and Pt/C for comparison. b) Time dependence of current density during HER with 12 h at fixed overpotential −0.174 V for $mMoO_3$ sample in 0.1 M KOH. Onset images: SEM images of $mMoO_3$ sample on Ni foam before and after stability test. c) Corresponding Tafel plots of $mMoO_3$ samples in 0.1 M KOH, along with bare Ni foam, $comMoO_3$, $mMoO_3$-T, and Pt/C for comparison. d) Polarization curves of all materials on carbon cloth electrode in 0.1 M H_2SO_4. e) Time dependence of current density during HER with 12 h at fixed overpotential −0.185 V for $mMoO_3$ sample in 0.1 M H_2SO_4. Onset images: SEM images of $mMoO_3$ sample on carbon cloth before and after stability test. f) Corresponding Tafel plots of $mMoO_3$ samples in 0.1 M H_2SO_4, along with bare carbon cloth, $comMoO_3$, and Pt/C for comparison.

www.MaterialsViews.com

ADVANCED
ENERGY
MATERIALS
www.advenergymat.de

FULL PAPER

Comparative Tafel plots derived from the polarization curves were studied to determine the Tafel slopes (Figure 5c). As a comparison, the commercial Pt/C sample shows a Tafel slope of 32 mV dec^{-1} in the lower overpotential range, corresponding to literature values.[42,43] A Tafel slope of ≈56 mV dec^{-1} for the mMoO$_3$ is comparable to the Pt/C sample under alkaline conditions. This is much lower than the value obtained for comMoO$_3$ (≈130 mV dec^{-1}), mMoO$_3$-T (≈110 mV dec^{-1}), or the bare Ni foam (≈101 mV dec^{-1}), indicating the enhancement of HER activity when using mMoO$_3$ as an electrocatalyst. The Tafel slope value of mMoO$_3$ is also comparable to previous reports for MoS$_x$ or WS$_x$ catalysts.[44,45]

Due to the reported poor corrosion stability of Mo based materials in acidic media, few studies in an acidic media were reported. The HER activity of all prepared catalysts was further tested under acidic conditions (0.1 M H$_2$SO$_4$) on C cloth. Shown in Figure 5d, bare C cloth substrate almost has no measurable HER activity within the potential window investigated. With the deposition of comMoO$_3$ on C cloth, a slightly enhanced HER activity can be observed (η = 422 mV for j = −10 mV cm^{-2}). In contrast, to achieve −10 mV cm^{-2} current density, mMoO$_3$ needs a much lower overpotential of 179 mV, which is much closer to the best HER electrocatalyst Pt/C (≈50 mV) under identical conditions. In Figure 5e, the stability of mMoO$_3$ was further investigated. No obvious current density change can be observed even after 12 h, which proves the excellent electrochemical stability of mesoporous MoO$_3$ in acidic media. No obvious morphology change can be observed thorough the comparison of SEM images (Figure 5e onset images, higher resolution images in Figure S10, Supporting Information) before and after stability tests, manifesting the high stability of mMoO$_3$ in acidic solution. The Tafel analysis of the HER polarization curves give rise to a slope of 72 mV dec^{-1} for the mMoO$_3$ catalyst (Figure 5f), which is much smaller than that for commercial MoO$_3$ (146 mV dec^{-1}) and much closer to that for commercial Pt/C (30 mV dec^{-1}), indicating a fast charge transfer process.

3. Discussion

3.1. The Presence of Oxygen Vacancies and Deficient MoO$_{3-x}$ Structure

The structure of a material plays a vital role for catalytic applications. To understand the relation between structure and catalytic activity, the formation of mesoporosity and an oxygen-deficient structure need to be discussed.

The facile synthesis method in this study has similarities and differences compared to previous reported studies. As mentioned above, Wu et al. descried a novel "oxygen extraction" approach to prepare oxygen deficient WO$_2$ materials. They employed ethylenediamine as a precursor and this is able to extract O-atoms from WO$_3$ to form NO$_x$ under Ar atmosphere. Similarly, we used PEO-b-PS as a reducing agent to create oxygen vacancies. However, no additional step is needed to extract oxygen in this study. The PEO-b-PS could act as a reducing agent to form Mo^{5+} and oxygen vacancies during the formation of the mesostructure. When Mo(VI) precursors

are bound to the oxyethylene groups of PEO chains during the coordination interaction, there is a reduction reaction to form Mo(V)-PEO complexes and assembly of inverse micelles through the THF evaporation (condensation) process. The formation of Mo(V) in the mMoO$_3$ sample may be due to the reducing ability of the PEO group in the PEO-b-PS template, which was previously reported in other studies.[46] Charge neutrality was then maintained by the presence of oxygen vacancies. By burning off the carbon based PEO-b-PS template, the formation of mesoporous and oxygen-deficient mMoO$_3$ material can be achieved simultaneously. Then the chemical formula of as-synthesized mesoporous MoO$_3$ materials could be identified as MoO$_{3-x}$, due to the presence of oxygen vacancies and the reduced Mo^{5+} species.

The nonstoichiometric structure of mMoO$_{3-x}$ was first indicated by XPS (Figure 3). XPS is regarded as a surface analysis technique, with an analysis depth of about 4 nm.[47,48] Shown in Figure 3a, comMoO$_3$ has an oxidation state of Mo^{6+}, while mMoO$_3$ shows an oxidation state of Mo^{5+}. The O 1s peak of mMoO$_3$ shifted to a lower binding energy level further supporting the change in the Mo—O bonds. The Mo^{5+} species observed in the mMoO$_3$ sample is considered mostly present on the surface (<10 nm). More evidence is provided from DR UV–vis (Figure 4a), and O$_2$ TPO (Figure 4b) characterization methods, which are discussed above. The significant color change of mMoO$_3$ before and after O$_2$ TPO treatment indicates the original presence of oxygen vacancies and subsequent filled vacancies after TPO.

3.2. Factors That Affect HER Activity

3.2.1. The Decisive Role of Structure

A decisive role of structure of materials for the HER activities has been reported in the literature. For example, a recent study of nanoporous MoS$_2$ synthesized by Kibsgaard et al. exhibited high HER activities due to a higher density of active surface sites.[49] However, the activity decreased at high currents due to the produced H$_2$ bubbles blocking the active sites inside the small porous network.[50] In this study, the design of large accessible pores (20–40 nm) of mMoO$_3$ is expected to improve HER activity without active sites being blocked.

In order to examine whether the mesostructure is able to improve the ion conductivity, we further conducted electrochemical impedance studies under both acidic and alkaline reaction conditions by using Electrochemical Impedance Spectroscopy (EIS), shown in Figure S11 (Supporting Information) with the equivalent circuit models also plotted (Figures S13 and S15, Supporting Information). The high-frequency intersection with the x-axis represents the uncompensated solution resistance (R_s, ohmic resistance), which is comparable for all catalysts (Tables S1 and S2, Supporting Information). The charge-transfer resistance (R_{ct}) in the electrochemical impedance spectrum, is related to the charge-transfer rate in HER. The EIS spectra for the comMoO$_3$ exhibit higher charge transfer resistance values under both alkaline and acidic conditions (R_{ct} = 66 and 12 Ω, respectively) than mMoO$_3$ catalyst. The R_{ct} of mMoO$_3$ are 43 and 6 Ω (in 0.1 M KOH and H$_2$SO$_4$, respectively),

FULL PAPER

indicating better conductivities and enhanced electrocatalytic performance than *com*MoO₃. This further suggests the vital role of mesoporosity in the HER process.

The mechanism of how the mesoporous structure promotes the charge transfer and ion conductivity is summarized as follows. Due to their pore shape, large pore size, high surface area, and high ion conductivity, mesoporous metal oxides have shown superior performances for electrochemical applications.[51,52] The mesopores, which make it easy to effectively transport guest molecules/ions to the active sites located in the internal particle, significantly enhance the charge transfer process during electrochemical reactions. In this study, in both alkaline and acidic media, the mesostructure contributes to the HER activity in two aspects. First of all, the mesopores with high surface area provide more active sites for HER. N_2 sorption measurements were applied to study the surface area of *com*MoO₃ and *m*MoO₃ materials. In Supporting Information (Figure S3), *m*MoO₃ (52 m² g⁻¹) possesses a much higher surface area than *com*MoO₃ (2 m² g⁻¹) by Brunauer–Emmett–Teller (BET) measurements. Generally, higher surface area comes with more active sites;[49] Second, mesopores facilitate the mass transport of fluids and the contact of reactant molecules/ions with active sites.[53,54] In the *com*MoO₃ system, without a porous structure, the electrolyte is only able to contact the surface of the bulk material, leading to the possible accumulation of electrons/ions/molecules on the surface and further decreases the reaction efficiency. In contrast, in the *m*MoO₃ system, mesopores act as open access to introduce fluids to contact with the internal structure, which effectively improves the mass transport without blocking active sites.[55] Thus, charge transfer and ion conductivity should be effectively promoted by the mesostructure.

Another property that may affect the HER activity is the oxygen-deficient structure. Structural defects are always considered as active sites in catalytic reactions. Similar HER, defects such as oxygen vacancies were regarded as active sites.[56] The contribution of oxygen vacancies to HER in this study can be directly observed. In Figure 5a, compared to the oxygen deficient *m*MoO₃ sample, the *m*MoO₃-T sample (without oxygen vacancies) exhibits much lower activity, indicating the significant role of oxygen vacancies during the HER process. The presence of oxygen vacancies enhances the interaction between oxygen-containing species and metal oxide surfaces.[57] In this study, oxygen vacancies may favor the adsorption of water molecules (or H_3O^+), which serve as electron acceptors, then lowering the HER energy barrier. In terms of DFT calculations (Figure 4c), the introduction of oxygen vacancies in MoO₃ gives rise to electrical conductivity. By reducing the metal cations, MoO₃ can be made to be semi-metallic due to filling of the *d*-band.[58] With the presence of oxygen vacancies, the hydrogen evolution reaction mechanism and pathway would be further affected.
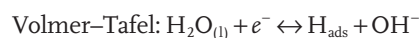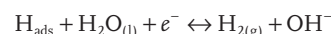
3.2.2. The Use of Ni Foam

Compared to *m*MoO₃ on Ni foam (Figure 5), *m*MoO₃ on GC exhibits lower activity (η = 138 mV vs 210 mV, Figure S9, Supporting Information). This indicates the Ni foam may improve the HER performance. The contributions of Ni foam may be summarized as two aspects. First, is that the large surface area of the 3D Ni foam could improve the catalyst loading. On Ni foam, *m*MoO₃ sample may possess more active surface area to contact with electrolyte compared to the GC electrodes; second, is the better dispersion of catalyst on Ni foam than on GC electrode. Catalyst may accumulate as a thick film on the GC electrode, which may limit the electrolyte diffusion and charge transport.
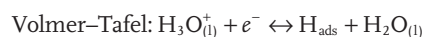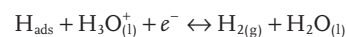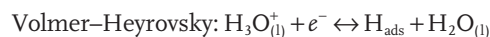
4. Proposed HER Mechanism

Generally, there are different mechanisms for HER in different conditions. The direct difference between alkaline and acidic mechanisms is the nature of the proton source [H_2O or H_3O^+(see equations below)].[59,60]

The HER in an alkaline media:

Volmer–Heyrovsky: $H_2O_{(l)} + e^- \leftrightarrow H_{ads} + OH^-$

$$H_{ads} + H_2O_{(l)} + e^- \leftrightarrow H_{2(g)} + OH^-$$

Volmer–Tafel: $H_2O_{(l)} + e^- \leftrightarrow H_{ads} + OH^-$

$$H_{ads} + H_{ads} \leftrightarrow H_{2(g)}$$

The HER in an acidic media:

Volmer–Heyrovsky: $H_3O^+_{(l)} + e^- \leftrightarrow H_{ads} + H_2O_{(l)}$

$$H_{ads} + H_3O^+_{(l)} + e^- \leftrightarrow H_{2(g)} + H_2O_{(l)}$$

Volmer–Tafel: $H_3O^+_{(l)} + e^- \leftrightarrow H_{ads} + H_2O_{(l)}$

$$H_{ads} + H_{ads} \leftrightarrow H_{2(g)}$$

After hydrogen atoms adsorbed on the surface of the catalyst, subsequent production of H_2 may occur via two different pathways. One part involves the Volmer–Heyrovsky mechanism (ion + atom reaction, Tafel slope ≈38 mV dec⁻¹), the adsorbed hydrogen atom (H_{ads}) accepts an electron and then combines with another proton source (H_2O or H_3O^+) to release H_2. Another part involves the direct combination of two H_{ads} (Tafel slope ≈29 mV dec⁻¹), which is called the Volmer–Tafel mechanism (combination reaction).[61]

To determine the predominant HER mechanism, the Tafel slope is a useful indicator by suggesting the additional voltage needed to increase the current density by tenfold. Generally, the smaller the value, the faster the HER rate. In Figure 5c, under alkaline conditions, the measured Tafel slope of Pt/C is 32 mV dec⁻¹, indicating a fast Volmer–Tafel process. For the *m*MoO₃ sample, a Tafel slope of 56 mV dec⁻¹ was observed, suggesting a fast HER rate via the Volmer–Heyrovsky process. With a Tafel slope close (or larger) to 116 mV dec⁻¹, the HER rate can be defined as a slow discharge reaction via the Volmer-Heyrovsky process, such as the Tafel slopes of bare Ni, bare C cloth, and *com*MoO₃ materials.[62] With the theoretical Tafel

Materials
Views
www.MaterialsViews.com

ADVANCED
ENERGY
MATERIALS
www.advenergymat.de

FULL PAPER

slope values, the HER mechanism under acidic conditions can be determined as well.

Based on the determination of the Volmer–Heyrovsky process, the HER pathway of mMoO$_3$ in 0.1 M KOH is then schematically described in **Figure 6** based on DFT calculations. Since α-MoO$_3$ has a layered structure and the site 1 oxygen vacancy (Figure 4d) on the top of the layer is preferred for an oxygen vacancy to form, we then constructed a MoO$_3$ slab based on these layers with the vacancy at site 1. In alkaline solution, the reaction pathway mainly involved H$_2$O (proton source) adsorption (intermediate 2, Figure 6), and reduction on the mMoO$_3$ surface to form hydrogen atoms adsorbed on the active site (intermediate 3), followed by H$_2$ formation (intermediate 4) and desorption (intermediate 5). The surface Mo^{5+} plays an important role during the formation of these five intermediates. The H$_2$O molecules are first adsorbed on the surface oxygen vacancies close to Mo^{5+} sites. The reduction of H$_2$O$_{ads}$, the formation of H$_{ads}$, and the release of H$_2$, OH$^-$ can only be effectively accomplished by a fast charge transfer process. The Mo^{5+} anions are able to donate electrons to form Mo^{6+} and then accept electrons to recover to Mo^{5+}. During the adsorption/desorption process on the oxygen vacancy sites, the charge balance can be maintained by the Mo^{5+}/Mo^{6+} pairs. The HER process can then be conducted by the cooperation between Mo^{5+} and oxygen vacancies.

Through DFT calculations, the oxygen vacancies close to Mo^{5+} were found to be the HER active sites. The intermediate (1) in Figure 6 is mMoO$_3$ with oxygen vacancies, surrounded by H$_2$O molecules in the electrolyte. The energy barrier for intermediate (2) with H$_2$O molecules adsorbed on the mMoO$_3$ surface is found to be 0.99 eV. As a comparison, MoO$_3$ material without any oxygen vacancies requires 1.69 eV (Figure S16, Supporting Information) to adsorb H$_2$O molecules. The presence of oxygen vacancies significantly lowered the energy barrier for H$_2$O adsorption. Intermediate (3) is the reduction of adsorbed H$_2$O molecules (H$_2$O$_{ads}$) and the formation of adsorbed hydrogen atoms (H$_{ads}$). Since the mMoO$_3$ material

followed the Volmer-Heyrovsky mechanism in terms of the experimental Tafel value (56 mV dec^{-1}), the H$_{ads}$ would combine with another adjacent H$_2$O$_{ads}$. The last step (intermediate 5) is the release of the formed H$_2$ molecule. The H$_2$ evolution energy barrier of mMoO$_3$ material with oxygen vacancies is much smaller compared to MoO$_3$ material without oxygen vacancies (1.29 vs 2.63 eV, Figure 6 vs Figure S16 in the Supporting Information). Overall, the mMoO$_3$ catalyst possesses suitable adsorption and desorption energy for H$_2$ evolution. The presence of oxygen vacancies could lower the kinetic energy barrier by facilitating H$_2$O adsorption and promoting H—H bond formation on two adjacent adsorbed H$_{ads}$ and H$_2$O$_{ads}$ species.

5. Conclusion

In summary, a new mesoporous, crystalline MoO$_{3-x}$ material has been successfully synthesized and identified as an active electrocatalyst for HER through experimental and theoretical (DFT) studies. Through a novel, cost effective, and flexible method of dissolving cheap molybdenum in H$_2$O$_2$ as precursor, combined with a PEO-b-PS template, the as-synthesized material has unique properties of mesoporosity and oxygen-deficiency. The as-synthesized mMoO$_3$ has a much larger surface area (52 m^2 g^{-1}) than comMoO$_3$ (2 m^2 g^{-1}), and shows outstanding performance in HER in both acidic and alkaline solution, without the assistance of carbon materials, extrinsic dopants, or other metal alloys. The calculated Tafel slope is as low as 56 mV dec^{-1} and the high activity can be maintained for more than 12 h. The key factors affecting HER activity are mesopores (20–40 nm) that facilitate the charge transfer, and the oxygen vacancies that narrow the bandgap leading to better conductivity. The oxygen vacancies that are close to Mo^{5+} are regarded as active sites for HER. All experimental and theoretical data suggest the HER performance highly depends on the unique structure of mMoO$_3$ materials. This study described a
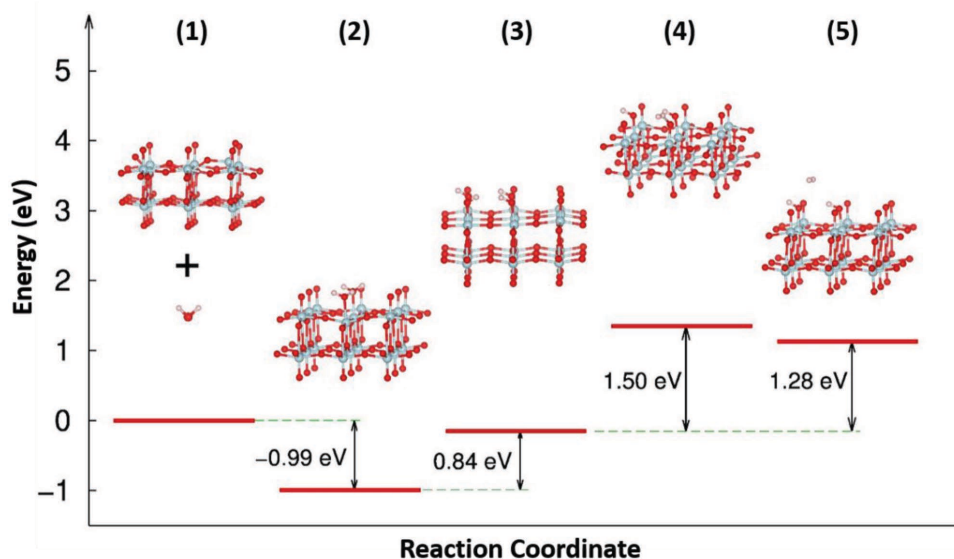
Figure 6. Proposed reaction pathway and the energy barrier profiles of mMoO$_3$ sample in 0.1 M KOH.

FULL PAPER

novel route to easily synthesize cheap, functional TMO materials with excellent HER activity and sheds light on the search for promising electrocatalysts for practical applications.

6. Experimental Section

Catalyst Preparation: In a typical synthesis, 0.26 g commercial MoO_3 (*com*MoO_3) was dissolved in 3 mL H_2O_2. After stirring for 2 d, a clear yellow gel was obtained. Then 0.1 g PEO-*b*-PS surfactant was dissolved in 7 mL THF solvent and stirred for 30 min. After all the surfactant was dissolved in THF, this solution was dropwise added to the clear yellow gel. After stirring for 30 min, the obtained homogeneous yellow gel was poured into a Petri dish to evaporate THF under ambient conditions. After 24 h, the obtained clear film was collected and calcined at 350 °C for 3 h under air. The blue greyish mesoporous MoO_3 calcined at 350 °C was prepared and labeled as *m*MoO_3.

Characterization: PXRD analyses were performed on a Rigaku Ultima IV diffractometer (Cu Kα radiation, $\lambda = 1.5406$ A) with an operating voltage of 40 kV and a current of 44 mA. Raman spectra were taken on a Renishaw 2000 Raman microscope with a wavelength of 514 nm, exposure time of 16, and accumulations of four times. Nitrogen (N_2) sorption experiments were conducted on a Quantachrome Autosorb-1-1C automated sorption system. The powders were degassed at 150 °C for 6 h prior to the measurements. The surface areas were calculated by the BET method, and the pore size distributions were calculated by the BJH method from the desorption isotherm. Morphological characterization was done using an FEI Nova NanoSEM 450 with an accelerating voltage of 2.0 kV. TEM, high-resolution TEM, and selected area electron diffraction were obtained in a JEOL 2010 UHR FasTEM operating at an accelerating voltage of 200 kV. The samples were prepared by dispersing the material in methanol. A drop of the dispersion was placed on a carbon coated copper grid and allowed to dry under ambient conditions. The powder samples were diluted in barium sulfate and pressed into the sample holder. XPS measurements were performed in a PHI model 590 spectrometer with multiprobes (ΦPhysical Electronics Industries Inc.), using Al Kα radiation ($\lambda = 1486.6$ eV) operated at 250 W. The shift of binding energy due to relative surface charging was corrected using the C 1s level at 284.6 eV as an internal standard. DR UV–vis spectra of the powder samples were collected with a diffuse reflectance apparatus attached on a Shimadzu UV-2450 UV–vis spectrophotometer. GPC measurements were performed using a Waters GPC-1 (1515 HPLC Pump and Waters 717Plus Autoinjector) equipped with a Varian 380-LC evaporative light scattering detector and a Waters 2487 dual absorbance detector, with three Jordi Gel fluorinated DVB columns (1–100 K, 2–10 K, and 1–500 Å). Proton nuclear magnetic resonance (1H NMR) spectra were recorded on a Bruker Avance 300 MHz spectrometer.

Electrochemical Studies: HER catalytic activity measurements were performed in a standard three-electrode system controlled by a CHI 660A electrochemistry workstation. The cell setup consisted of a working electrode (Ni foam or carbon cloth) coated with the sample, an SCE reference electrode, a graphite rod electrode, and 0.1 M KOH or H_2SO_4 solution as the electrolyte. The reference was calibrated against and converted to an RHE. Linear sweep voltammetry was carried out at 5 mV s^{-1} for the polarization curves. All polarization curves were iR-corrected. The working electrode was prepared as follows: 10 mg of active material sample and 10 mg of carbon (VulcanXC-72) were dispersed in a mixture of deionized distilled water and isopropanol (4 mL:1 mL) and sonicated for 3 min, followed by adding 20 µL of polytetrafluoroethylene solution (60% in water, Sigma) and sonicating for 5 min to form a suspension. A 20 µL suspension was deposited onto Ni foam or carbon cloth using a micropipette. The catalyst loadings were 0.2 mg cm^{-2}.

Supporting Information

Supporting Information is available from the Wiley Online Library or from the author.

[1] C. C. L. McCrory, S. Jung, J. C. Peters, T. F. Jaramillo, *J. Am. Chem. Soc.* **2013**, *135*, 16977.

[2] J. Suntivich, K. J. May, H. A. Gasteiger, J. B. Goodenough, Y. Shao-Horn, *Science* **2011**, *334*, 1383.

[3] D.-Y. Wang, M. Gong, H.-L. Chou, C.-J. Pan, H.-A. Chen, Y. Wu, M.-C. Lin, M. Guan, J. Yang, C.-W. Chen, Y.-L. Wang, B.-J. Hwang, C.-C. Chen, H. Dai, *J. Am. Chem. Soc.* **2015**, *137*, 1587.

[4] S. Xu, D. Li, P. Wu, *Adv. Funct. Mater.* **2015**, *25*, 1127.

[5] M. Shalom, S. Gimenez, F. Schipper, I. Herraiz-Cardona, J. Bisquert, M. Antonietti, *Angew. Chem.* **2014**, *126*, 3728.

[6] R. Wu, J. Zhang, Y. Shi, D. Liu, B. Zhang, *J. Am. Chem. Soc.* **2015**, *137*, 6983.

[7] D. Kong, H. Wang, Z. Lu, Y. Cui, *J. Am. Chem. Soc.* **2014**, *136*, 4897.

[8] Y. Zhao, K. Kamiya, K. Hashimoto, S. Nakanishi, *J. Am. Chem. Soc.* **2015**, *137*, 110.

[9] B. Cao, G. M. Veith, J. C. Neuefeind, R. R. Adzic, P. G. Khalifah, *J. Am. Chem. Soc.* **2013**, *135*, 19186.

[10] F. H. Saadi, A. I. Carim, J. M. Velazquez, J. H. Baricuatro, C. C. L. McCrory, M. P. Soriaga, N. S. Lewis, *ACS Catal.* **2014**, *4*, 2866.

[11] Z. Chen, D. Cummins, B. N. Reinecke, E. Clark, M. K. Sunkara, T. F. Jaramillo, *Nano Lett.* **2011**, *11*, 4168.

[12] B. Hinnemann, P. G. Moses, J. Bonde, K. P. Jørgensen, J. H. Nielsen, S. Horch, I. Chorkendorff, J. K. Nørskov, *J. Am. Chem. Soc.* **2005**, *127*, 5308.

[13] X.-R. Shi, J. Wang, K. Hermann, *J. Phys. Chem. C* **2010**, *114*, 6791.

[14] Y. Shi, B. Guo, S. A. Corr, Q. Shi, Y.-S. Hu, K. R. Heier, L. Chen, R. Seshadri, G. D. Stucky, *Nano Lett.* **2009**, *9*, 4215.

[15] T. Brezesinski, J. Wang, S. H. Tolbert, B. Dunn, *Nat. Mater.* **2010**, *9*, 146.

[16] L. Q. Mai, B. Hu, W. Chen, Y. Y. Qi, C. S. Lao, R. S. Yang, Y. Dai, Z. L. Wang, *Adv. Mater.* **2007**, *19*, 3712.

[17] B. Liu, C.-H. Kuo, J. Chen, Z. Luo, S. Thanneeru, W. Li, W. Song, S. Biswas, S. L. Suib, J. He, *Angew. Chem.* **2015**, *127*, 9189.

[18] J. Rosen, G. S. Hutchings, F. Jiao, *J. Am. Chem. Soc.* **2013**, *135*, 4516.

[19] W. Zhou, W. Li, J.-Q. Wang, Y. Qu, Y. Yang, Y. Xie, K. Zhang, L. Wang, H. Fu, D. Zhao, *J. Am. Chem. Soc.* **2014**, *136*, 9280.

[20] R. Miao, Z. Luo, W. Zhong, S.-Y. Chen, T. Jiang, B. Dutta, Y. Nasr, Y. Zhang, S. L. Suib, *Appl. Catal., B* **2016**, *189*, 26.

[21] Q. Wu, R. van de Krol, *J. Am. Chem. Soc.* **2012**, *134*, 9369.

[22] J.-H. Lee, R. Black, G. Popov, E. Pomerantseva, F. Nan, G. A. Botton, L. F. Nazar, *Energy Environ. Sci.* **2012**, *5*, 9558.

[23] J. Wang, Z. Wang, B. Huang, Y. Ma, Y. Liu, X. Qin, X. Zhang, Y. Dai, *ACS Appl. Mater. Interfaces* **2012**, *4*, 4024.

[24] C. Di Valentin, G. Pacchioni, *Acc. Chem. Res.* **2014**, *47*, 3233.

[25] S. Tanisaki, *J. Phys. Soc. Jpn.* **1960**, *15*, 573.

[26] C. J. Machiels, W. H. Cheng, U. Chowdhry, W. E. Farneth, F. Hong, E. M. Mc Carron, A. W. Sleight, *Appl. Catal.* **1986**, *25*, 249.

[27] H. Cheng, T. Kamegawa, K. Mori, H. Yamashita, *Angew. Chem., Int. Ed. Engl.* **2014**, *53*, 2910.

[28] T. M. McEvoy, K. J. Stevenson, J. T. Hupp, X. Dang, *Langmuir* **2003**, *19*, 4316.

www.MaterialsViews.com

ADVANCED
ENERGY
MATERIALS
www.advenergymat.de

FULL PAPER

[29] L. Cai, P. M. Rao, X. Zheng, *Nano Lett.* **2011**, *11*, 872.

[30] M. Dieterle, G. Mestl, *Phys. Chem. Chem. Phys.* **2002**, *4*, 822.

[31] R. Liang, H. Cao, D. Qian, *Chem. Commun.* **2011**, *47*, 10305.

[32] M. Vasilopoulou, A. M. Douvas, D. G. Georgiadou, L. C. Palilis, S. Kennou, L. Sygellou, A. Soultati, I. Kostis, G. Papadimitropoulos, D. Davazoglou, P. Argitis, *J. Am. Chem. Soc.* **2012**, *134*, 16178.

[33] D. O. Scanlon, G. W. Watson, D. J. Payne, G. R. Atkinson, R. G. Egdell, D. S. L. Law, *J. Phys. Chem. C* **2010**, *114*, 4636.

[34] Z. Luo, A. S. Poyraz, C.-H. Kuo, R. Miao, Y. Meng, S.-Y. Chen, T. Jiang, C. Wenos, S. L. Suib, *Chem. Mater.* **2015**, *27*, 6.

[35] J. Światowska-Mrowiecka, S. de Diesbach, V. Maurice, S. Zanna, L. Klein, E. Briand, I. Vickridge, P. Marcus, *J. Phys. Chem. C* **2008**, *112*, 11050.

[36] Q. Kang, J. Cao, Y. Zhang, L. Liu, H. Xu, J. Ye, *J. Mater. Chem. A* **2013**, *1*, 5766.

[37] H. Chen, Z. Wei, K. Yan, Y. Bai, S. Yang, *J. Phys. Chem. Lett.* **2014**, *5*, 2890.

[38] K. Manthiram, A. P. Alivisatos, *J. Am. Chem. Soc.* **2012**, *134*, 3995.

[39] T. R. Gordon, M. Cargnello, T. Paik, F. Mangolini, R. T. Weber, P. Fornasiero, C. B. Murray, *J. Am. Chem. Soc.* **2012**, *134*, 6751.

[40] F. Lei, Y. Sun, K. Liu, S. Gao, L. Liang, B. Pan, Y. Xie, *J. Am. Chem. Soc.* **2014**, *136*, 6826.

[41] W. Bi, C. Ye, C. Xiao, W. Tong, X. Zhang, W. Shao, Y. Xie, *Small* **2014**, *10*, 2820.

[42] X. Fan, H. Zhou, X. Guo, *ACS Nano* **2015**, *9*, 5125.

[43] H. Zhang, Z. Ma, J. Duan, H. Liu, G. Liu, T. Wang, K. Chang, M. Li, L. Shi, X. Meng, K. Wu, J. Ye, *ACS Nano* **2015**, *10*, 684.

[44] A. J. Smith, Y.-H. Chang, K. Raidongia, T.-Y. Chen, L.-J. Li, J. Huang, *Adv. Energy Mater.* **2014**, *4*, 1400398.

[45] J. Lin, Z. Peng, G. Wang, D. Zakhidov, E. Larios, M. J. Yacaman, J. M. Tour, *Adv. Energy Mater.* **2014**, *4*, 1301875.

[46] L. Longenberger, G. Mills, *J. Phys. Chem.* **1995**, *99*, 475.

[47] J. T. Cherian, R. M. Fisher, D. G. Castner, R. R. Dellwo, *J. Mater. Sci.* **2001**, *36*, 4189.

[48] L. Fras, L.-S. Johansson, P. Stenius, J. Laine, K. Stana-Kleinschek, V. Ribitsch, *Colloids Surf., A* **2005**, *260*, 101.

[49] J. Kibsgaard, Z. Chen, B. N. Reinecke, T. F. Jaramillo, *Nat. Mater.* **2012**, *11*, 963.

[50] Q. Lu, G. S. Hutchings, W. Yu, Y. Zhou, R. V Forest, R. Tao, J. Rosen, B. T. Yonemoto, Z. Cao, H. Zheng, J. Q. Xiao, F. Jiao, J. G. Chen, *Nat. Commun.* **2015**, *6*, 6567.

[51] T. Sun, C. Zhang, J. Chen, Y. Yan, A. A. Zakhidov, R. H. Baughman, L. Xu, *J. Mater. Chem. A* **2015**, *3*, 11367.

[52] T. Jiang, A. S. Poyraz, A. Iyer, Y. Zhang, Z. Luo, W. Zhong, R. Miao, A. M. El-Sawy, C. J. Guild, Y. Sun, D. A. Kriz, S. L. Suib, *J. Phys. Chem. C* **2015**, *119*, 10454.

[53] O.-H. Kim, Y.-H. Cho, S. H. Kang, H.-Y. Park, M. Kim, J. W. Lim, D. Y. Chung, M. J. Lee, H. Choe, Y.-E. Sung, *Nat. Commun.* **2013**, *4*, 2473.

[54] T. Y. Ma, S. Dai, M. Jaroniec, S. Z. Qiao, *J. Am. Chem. Soc.* **2014**, *136*, 13925.

[55] Z. Xing, Q. Liu, A. M. Asiri, X. Sun, *Adv. Mater.* **2014**, *26*, 5702.

[56] J. Xie, J. Zhang, S. Li, R. Wang, X. Sun, M. Zhou, J. Zhou, X. W. D. Lou, Y. Xie, *Adv. Mater.* **2013**, *25*, 5807.

[57] F. Cheng, T. Zhang, Y. Zhang, J. Du, X. Han, J. Chen, *Angew. Chem., Int. Ed. Engl.* **2013**, *52*, 2474.

[58] M. Dieterle, G. Weinberg, G. Mestl, *Phys. Chem. Chem. Phys.* **2002**, *4*, 812.

[59] E. Skúlason, V. Tripkovic, M. E. Björketun, S. Gudmundsdóttir, G. Karlberg, J. Rossmeisl, T. Bligaard, H. Jónsson, J. K. Nørskov, *J. Phys. Chem. C* **2010**, *114*, 18182.

[60] B. E. Conway, B. V. Tilak, *Electrochim. Acta* **2002**, *47*, 3571.

[61] C. G. Morales-Guio, L.-A. Stern, X. Hu, *Chem. Soc. Rev.* **2014**, *43*, 6555.

[62] J. O. Bockris, E. C. Potter, *J. Electrochem. Soc.* **1952**, *99*, 169.